
This copy is for your personal, non-commercial use only.

If you wish to distribute this article to others, you can order high-quality copies for your colleagues, clients, or customers by [clicking here](#).

Permission to republish or repurpose articles or portions of articles can be obtained by following the guidelines [here](#).

The following resources related to this article are available online at www.sciencemag.org (this information is current as of August 28, 2011):

Updated information and services, including high-resolution figures, can be found in the online version of this article at:

<http://www.sciencemag.org/content/326/5955/964.full.html>

A list of selected additional articles on the Science Web sites **related to this article** can be found at:

<http://www.sciencemag.org/content/326/5955/964.full.html#related>

This article **cites 15 articles**, 4 of which can be accessed free:

<http://www.sciencemag.org/content/326/5955/964.full.html#ref-list-1>

This article has been **cited by** 8 article(s) on the ISI Web of Science

This article has been **cited by** 5 articles hosted by HighWire Press; see:

<http://www.sciencemag.org/content/326/5955/964.full.html#related-urls>

This article appears in the following **subject collections**:

Planetary Science

http://www.sciencemag.org/cgi/collection/planet_sci

Identifying the ribbon over a broad energy range has implications for its stability. ENAs with energies of 1 keV take ~1.1 years to propagate from 100 AU to Earth, whereas ENAs with energies of 0.2 keV take ~2.4 years to make the same journey. Thus, the ribbon must exist over at least ~1 year.

References and Notes

1. D. J. McComas *et al.*, *Space Sci. Rev.* 10.1007/s11214-009-9499-4 (2009).

2. D. J. McComas *et al.*, *Science* **326**, 959 (2009); published online 15 October 2009 (10.1126/science.1180906).
 3. E. Möbius *et al.*, *Science* **326**, xxx (2009); published online 15 October 2009 (10.1126/science.1180971).
 4. S. A. Fuselier *et al.*, *Space Sci. Rev.* 10.1007/s11214-009-9495-8 (2009).
 5. H. O. Funsten *et al.*, *Science* **326**, 964 (2009); published online 15 October 2009 (10.1126/science.1180927).
 6. N. A. Schwadron *et al.*, *Science* **326**, 966 (2009); published online 15 October 2009 (10.1126/science.1180986).

7. These results from the IBEX mission are a tribute to the hard work of many scientists and engineers. Work at Lockheed Martin was funded by NASA through sub-contract from Southwest Research Institute.

24 August 2009; accepted 2 October 2009

Published online 15 October 2009;
 10.1126/science.1180981

Include this information when citing this paper.

Structures and Spectral Variations of the Outer Heliosphere in IBEX Energetic Neutral Atom Maps

H. O. Funsten,^{1*} F. Allegrini,^{2,3} G. B. Crew,⁴ R. DeMajistre,⁵ P. C. Frisch,⁶ S. A. Fuselier,⁷ M. Gruntman,⁸ P. Janzen,⁹ D. J. McComas,^{2,3} E. Möbius,¹⁰ B. Randol,^{3,2} D. B. Reisenfeld,⁹ E. C. Roelof,⁵ N. A. Schwadron¹¹

The Interstellar Boundary Explorer (IBEX) has obtained all-sky images of energetic neutral atoms emitted from the heliosheath, located between the solar wind termination shock and the local interstellar medium (LISM). These flux maps reveal distinct nonthermal (0.2 to 6 kilo-electron volts) heliosheath proton populations with spectral signatures ordered predominantly by ecliptic latitude. The maps show a globally distributed population of termination-shock-heated protons and a superimposed ribbonlike feature that forms a circular arc in the sky centered on ecliptic coordinate (longitude λ , latitude β) = (221°, 39°), probably near the direction of the LISM magnetic field. Over the IBEX energy range, the ribbon's nonthermal ion pressure multiplied by its radial thickness is in the range of 70 to 100 picodynes per square centimeter AU (AU, astronomical unit), which is significantly larger than the 30 to 60 picodynes per square centimeter AU of the globally distributed population.

Energetic neutral atoms (ENAs) are formed when energetic ions in the heliosheath, predominantly H^+ , are neutralized by charge exchange with the neutral component of the interstellar gas, predominantly H^0 . Imaging and spectroscopy of these ENAs are used to remotely survey the structure and dynamics of heliosheath plasmas (1, 2). The IBEX-Lo (3) and IBEX-Hi imagers (4) on the Interstellar Boundary Explorer (IBEX) mission (5) measure heliosheath ENAs over the energy range from ~0.2 to 6 keV. The IBEX-Hi and IBEX-Lo all-sky maps show a ribbon (6, 7) that was not anticipated by current models of the structure and dynamics of the interaction region (8). The ribbon is superim-

posed on a globally distributed ENA flux that varies slowly over the sky (6). Here we characterize the underlying plasma structures in the heliosheath by analyzing the spectral index derived from the ENA flux maps (6) both inside and outside the ribbon.

The ENA spectra show two distinct spectral shapes independent of ecliptic longitude λ (Fig. 1, A to C). The blue (north) and red (south) spectra are similar in shape, even though their corresponding intensities vary over a factor of ~2 to 3, with higher intensities in the ribbon. They all exhibit a conspicuous flattening of their slopes for energies >1 keV, which is the characteristic energy range for pickup ions in the fast solar wind that are further heated at the termination shock (9). At each energy passband, the ENA fluxes of all north and south spectra of Fig. 1, A to C (except for the northern tail, which contains the ribbon), are similar, with average fluxes of 192, 79, 30, 17, and 8.7 $cm^{-2} s^{-1} sr^{-1} keV^{-1}$ at energy passbands centered at 0.7, 1.1, 1.7, 2.7, and 4.3 keV, respectively, and standard deviations within 10% of the average flux values at each energy.

In contrast to the high-latitude spectra, the smooth low-latitude (green) spectra can be approximated as a power law spectrum with a single spectral index κ (8). This applies even in the ribbon, which exhibits a larger overall in-

tensity but a similar single slope as compared to nonribbon spectra (Fig. 2, A and C). The value of κ at low latitudes shows a weak trend with longitude (Fig. 1D), with fits of the data over the nine energy channels yielding $\kappa = 1.5$ for the nose and $\kappa = 2.1$ for the tail. The nose and tail spectral shapes are also slightly but consistently different, possibly resulting from longer line-of-sight (LOS) integrations of low-energy ions toward the tail. Another exception is the spectrum in the direction of Voyager 1 (6), which is more characteristic of high-latitude spectra.

The spectral index κ at higher energies is predominantly ordered by ecliptic latitude β (Fig. 2, A and B). The spectral indexes within the ribbon nearly overlap with and show the same strong latitude dependence as the globally distributed flux outside the ribbon. For the globally distributed flux that does not include the ribbon, the average spectral index at low latitudes ($-30^\circ \leq \beta \leq 30^\circ$) is $\kappa = 1.95 \pm 0.09$ at 1.7 keV and $\kappa = 1.91 \pm 0.07$ at 2.7 keV, and at high latitudes ($\beta \leq -54^\circ$, $\beta \geq 54^\circ$) is $\kappa = 1.49 \pm 0.05$ and $\kappa = 1.36 \pm 0.08$, respectively, revealing a distinctly different higher-energy ion population at high latitude.

These observations show that the global characteristics of nonthermal heliosheath ions are ordered predominantly by ecliptic latitude, regardless of whether they reside inside or outside of the ribbon. Because ecliptic latitude is almost indistinguishable from heliographic latitude, this spectral signature is probably imposed by the latitude dependence of the solar wind, whose transition from slow (equatorial) to fast (polar) solar wind in the outer heliosphere occurs at mid-latitudes throughout the present minimum phase of the solar cycle (10). It also suggests that the intensity features of the ribbon are not produced by local heliosheath acceleration processes that would presumably impose a different spectral signature associated only with these higher fluxes. If the solar wind orders the spectral characteristics of heliosheath plasma, we expect temporal variation of the globally distributed flux, and possibly structures such as the ribbon, caused by the changing solar wind pattern throughout the 11-year (and possibly 22-year) solar cycle.

We divided the ribbon into three regions based on differences in spectral signature (Fig. 2, C and D). The spectra of regions 1 and 3 are consistent with the spectral signatures of low- and high-latitude regions, respectively (Fig. 1, A

¹Los Alamos National Laboratory, Los Alamos, NM 87545, USA.

²Southwest Research Institute, San Antonio, TX 78228, USA.

³University of Texas at San Antonio, San Antonio, TX 78249, USA.

⁴Massachusetts Institute of Technology, Cambridge, MA 02139, USA.

⁵Applied Physics Laboratory, Johns Hopkins University, Laurel, MD 20723, USA.

⁶University of Chicago, Chicago, IL 60637, USA.

⁷Lockheed Martin Advanced Technology Center, Palo Alto, CA 94304, USA.

⁸University of Southern California, Los Angeles, CA 90089-1192, USA.

⁹University of Montana, Missoula, MT 59812, USA.

¹⁰University of New Hampshire, Morse Hall, Durham, NH 03824, USA.

¹¹Boston University, Boston, MA, 02215, USA.

*To whom correspondence should be addressed. E-mail: hfunsten@lanl.gov

to C). However, region 2 is a highly localized knot of ENA emission that is apparent in the ENA flux maps and lies within -30° to 12° longitude and 38° to 72° latitude. The flux is enhanced relative to region 3 at 1.7 and 2.7 keV and is highly variable over small spatial scales. By 4.3 keV, the fluxes converge to the values of region 3. These observations suggest the presence of a dynamic process whose characteristic signature lies in the energy range from ~ 1 to 2.7 keV. Region 2 lies toward the northern extent of the interaction region of fast and slow solar wind and might, for example, arise from preferential ion acceleration near the termination shock (11).

The ribbon is probably associated with an enhanced plasma pressure, consistent with plasma flow away from the ribbon measured at the Voyager spacecraft, whose locations straddle the ribbon (6). Along a single LOS, heliospheric ENAs are emitted from a source region with average thickness L . The energetic ions over this emission region exert an average nonthermal partial pressure ΔP_{ion} . We estimate the product $\Delta P_{ion}L$ by assuming an isotropic ion distribution of intensity $j_{ion}(E)$. The average ENA flux along the LOS as measured by IBEX is $j_{ENA}(E) = \sigma_{10}(E)n_H j_{ion}(E)L$, where $\sigma_{10}(E)$ is the charge exchange cross section for $H^+ + H^0 \rightarrow H + H^0$ (12) and $n_H \approx 0.1 \text{ cm}^{-3}$ is the lower-bound density of H^0 from the local interstellar medium (LISM) along the LOS (13). The ion partial pressure over an energy range ΔE (such as an IBEX energy passband) is $\Delta P_{ion} = (4\pi/3)j_{ion}(E)p_{ion}\Delta E$, where p_{ion} is the ion momentum.

Over the energy range from 0.2 to 6.0 keV, the ribbon dominates $\Delta P_{ion}L$, ranging from 70 to 110 pdynes cm^{-2} AU as compared to 30 to 60 pdynes cm^{-2} AU for the globally distributed flux (Fig. 3). The larger $\Delta P_{ion}L$ in the ribbon could be from higher ion pressure, a thicker plasma source region, or a combination of both. Using $\Delta P_{ion}L \approx 100$ pdynes cm^{-2} AU and assuming that the ribbon radial thickness $L \approx 50$ AU is similar to its apparent 20° width (9) at 150 AU, the average IBEX partial pressure in the ribbon is $\Delta P_{ion} \approx 2$ pdynes cm^{-2} (~ 0.2 pPa), which is comparable to the estimated external forces exerted by the LISM (8).

The pressure produced by the nonthermal ion distribution probably governs the structure, dynamics, and geometry of the heliosheath. The region of highest $\Delta P_{ion}L$ (~ 100 pdynes cm^{-2} AU) follows a circular arc whose center is the likely direction of the LISM magnetic field direction. The arc center, derived by linear regression using the latitude of the $6^\circ \times 6^\circ$ pixel having maximum $\Delta P_{ion}L$ at each longitude, lies along a LOS through ecliptic $(\lambda, \beta) = (221^\circ, 39^\circ)$, which is $\sim 46^\circ$ from the heliospheric nose. The mean angle between the LOS of the arc center and the LOS of the $\Delta P_{ion}L$ maxima is $71.6^\circ \pm 3.9^\circ$. The three-dimensional geometry of the regions of enhanced $\Delta P_{ion}L$ is therefore a cone through the heliosheath with the Sun as its apex. The ribbon's arc of high $\Delta P_{ion}L$ is con-

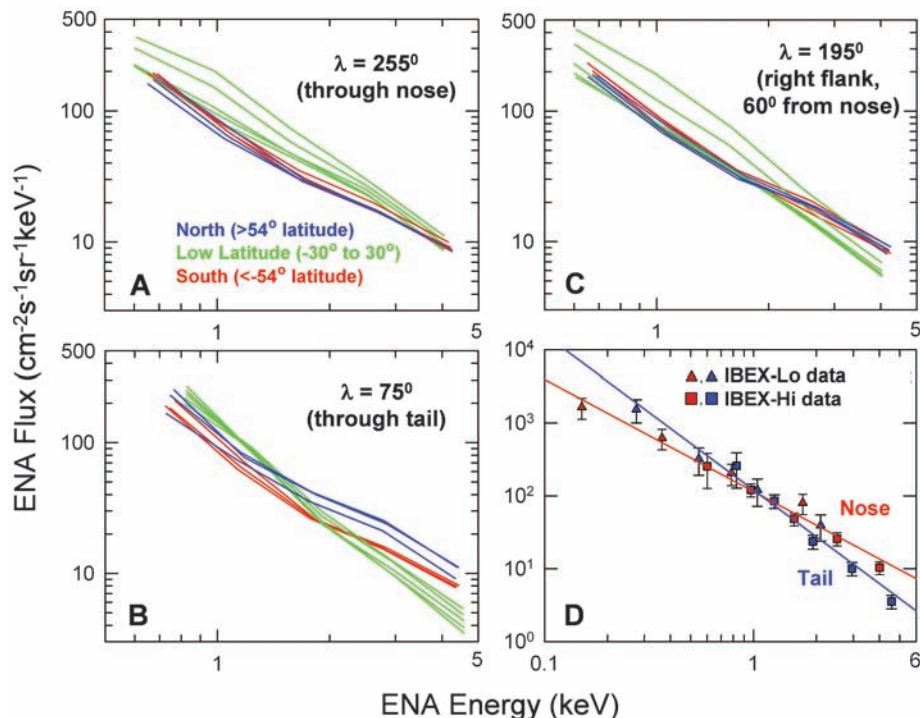


Fig. 1. ENA spectra from several regions. Measurements were transformed into the rest frame of the Sun. Average fluxes from 24° longitude \times 12° latitude areas in longitudinal slices centered on the heliospheric (A) nose ($\lambda = 255^\circ$), (B) tail, and (C) right flank (60° from the nose) are shown. The green spectra are from low ecliptic latitudes ($-30^\circ \leq \beta \leq 30^\circ$), and the blue and red spectra are from northern ($\beta \geq 54^\circ$) and southern ($\beta \leq -54^\circ$) polar regions, respectively. The low-latitude spectra with the highest flux in (A) and (C) are from latitudes centered on -12° and -24° and contain the ribbon. The north latitude spectra with the highest flux in (B) also contain the ribbon. (D) Spectra from $20^\circ \times 20^\circ$ regions centered on the nose (red) and tail (blue) and fit over nine energy passbands of IBEX. Typical error bars in (D) represent counting statistics and systematic errors of $\pm 20\%$ for IBEX-Hi and $\pm 30\%$ for IBEX-Lo.

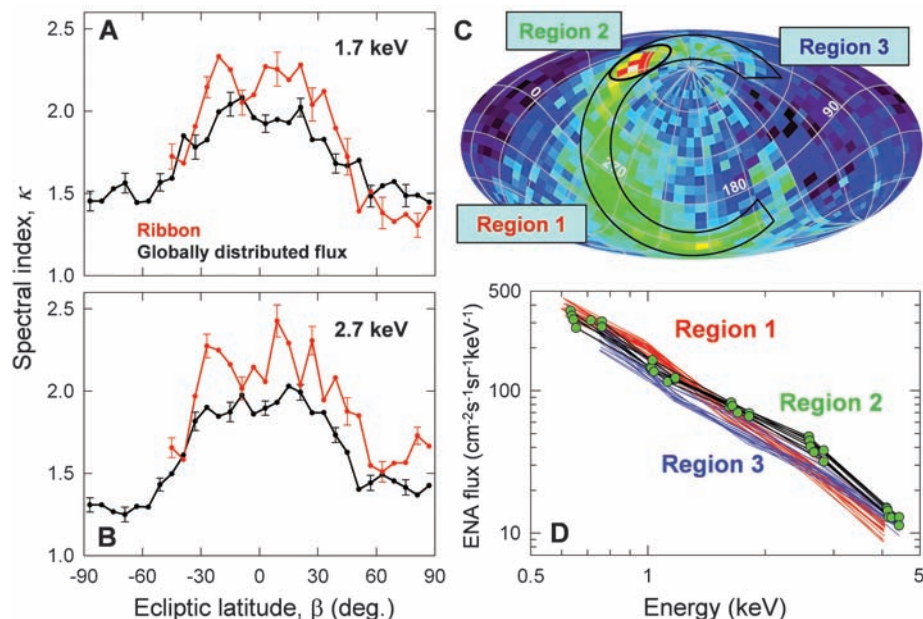
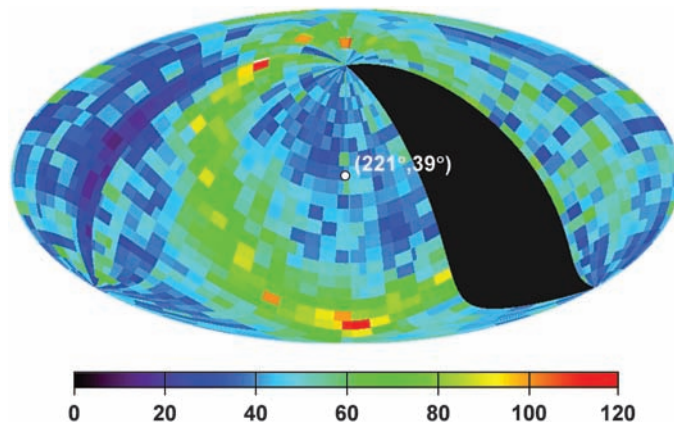


Fig. 2. Global spectral variation with latitude and within the ribbon. The variance-weighted mean of κ for the ribbon (red) and globally distributed flux outside the ribbon (black) are calculated using three adjacent IBEX-Hi energy passbands centered on (A) 1.7 keV and (B) 2.7 keV. Error bars represent errors in the weighted mean. The 2.7-keV ENA flux map (C) is centered on ecliptic $(\lambda, \beta) = (221^\circ, 39^\circ)$ and shows three regions of the ribbon. (D) Spectra from these three regions are derived from the average ENA flux in areas 6° in longitude by 18° in latitude centered on the ribbon.

Fig. 3. The product of the ion pressure ΔP_{ion} in the heliosheath and the radial thickness L of the ENA emission in units of p dynes cm^{-2} AU over the energy range from 0.2 to 6 keV that includes the 0.44-keV passband of IBEX-Lo and the 0.7-, 1.1-, 1.7-, 2.7-, and 4.3-keV passbands of IBEX-Hi. The black swath is data removed because of poor statistics in the IBEX-Lo energy passband.



sistent with the locus of points for which the external LISM magnetic field vector lies transverse to the IBEX LOS, a region of comparably strong dynamic and magnetic force exerted by the LISM (6, 8). The likely LOS direction $(\lambda, \beta) = (221^\circ, 39^\circ)$ parallel to the interstellar magnetic field derived here lies within the range $210^\circ \leq \lambda \leq 240^\circ$ and $30^\circ \leq \beta \leq 60^\circ$, obtained using the offset in flow directions between interstellar H^0 and He^0 (14), and is consistent with the direc-

tion inferred from 2- to 3-kHz radio emissions measured at the Voyager spacecraft (15).

References and Notes

1. M. Gruntman, *Rev. Sci. Instrum.* **68**, 3617 (1997).
2. M. Gruntman et al., *J. Geophys. Res.* **106**, 15767 (2001).
3. S. A. Fuselier et al., *Space Sci. Rev.*, 10.1007/s11214-009-9495-8 (2009).
4. H. O. Funsten et al., *Space Sci. Rev.*, 10.1007/s11214-009-9504-y (2009).

5. D. J. McComas et al., *Space Sci. Rev.*, 10.1007/s11214-009-9499-4 (2009).
6. D. J. McComas et al., *Science* **326**, 959 (2009); published online 15 October 2009 (10.1126/science.1180906).
7. S. A. Fuselier et al., *Science* **326**, 962 (2009); published online 15 October 2009 (10.1126/science.1180981).
8. N. A. Schwadron et al., *Science* **326**, 966 (2009); published online 15 October 2009 (10.1126/science.1180986).
9. R. B. Decker et al., *Nature* **454**, 67 (2008).
10. D. J. McComas et al., *Geophys. Res. Lett.* **25**, 1 (1998).
11. N. A. Schwadron, D. J. McComas, *Geophys. Res. Lett.* **30**, 1587 (2003).
12. B. G. Lindsay, R. F. Stebbings, *J. Geophys. Res.* **110**, A12213 (2005).
13. H. R. Müller, G. P. Zank, *J. Geophys. Res.* **109**, A07104 (2004).
14. R. Lallement et al., *Science* **307**, 1447 (2005).
15. D. A. Gunnert, W. S. Kurth, I. H. Cairns, J. Mitchell, *AIP Conf. Proc.* **858**, 129 (2006).
16. We thank all the IBEX team members, who enabled the success of IBEX through their individual talents, dedication, and hard work. This work was funded by the NASA Explorer Program. Work at Los Alamos was performed under the auspices of the U.S. Department of Energy.

21 August 2009; accepted 2 October 2009
Published online 15 October 2009;
10.1126/science.1180927

Include this information when citing this paper.

Comparison of Interstellar Boundary Explorer Observations with 3D Global Heliospheric Models

N. A. Schwadron,^{1,13*} M. Bzowski,² G. B. Crew,³ M. Gruntman,⁴ H. Fahr,⁵ H. Fichtner,⁶ P. C. Frisch,⁷ H. O. Funsten,⁸ S. Fuselier,⁹ J. Heerikhuisen,¹⁰ V. Izmodenov,¹¹ H. Kucharek,¹² M. Lee,¹² G. Livadiotis,¹³ D. J. McComas,^{13,14} E. Moebius,¹² T. Moore,¹⁵ J. Mukherjee,¹³ N.V. Pogorelov,¹⁰ C. Prested,¹ D. Reisenfeld,¹⁶ E. Roelof,¹⁷ G.P. Zank¹⁰

Simulations of energetic neutral atom (ENA) maps predict flux magnitudes that are, in some cases, similar to those observed by the Interstellar Boundary Explorer (IBEX) spacecraft, but they miss the ribbon. Our model of the heliosphere indicates that the local interstellar medium (LISM) magnetic field (B_{LISM}) is transverse to the line of sight (LOS) along the ribbon, suggesting that the ribbon may carry its imprint. The force-per-unit area on the heliopause from field line draping and the LISM ram pressure is comparable with the ribbon pressure if the LOS ~ 30 to 60 astronomical units and $B_{\text{LISM}} \sim 2.5$ microgauss. Although various models have advantages in accounting for some of the observations, no model can explain all the dominant features, which probably requires a substantial change in our understanding of the processes that shape our heliosphere.

Previous models of energetic neutral atom (ENA) maps (I) provide limits on possible emission patterns depending on the assumed proton distributions in the heliosheath. Models with assumed Maxwellian distributions in the heliosheath show a broad enhanced emission region near the nose where the flow stagnates, whereas highly nonthermal distributions dominated by pickup ions (PUIs) show higher intensities in the sidewind direction and toward

the tail where the line-of-sight (LOS) integrations across the heliosheath extended over large distances [hundreds of astronomical units (AU)]. Three-dimensional (3D) models incorporating a κ distribution, defined in (2), as a distribution with a Gaussian-like core and a power-law tail, manifest structure influenced by the local interstellar medium (LISM) magnetic field (B_{LISM}) (3). The observed difference inside the termination shock (TS) between in-

terstellar helium flow and the hydrogen flow (4), which interacts more strongly with the outer heliosheath plasma (beyond the heliopause), suggests that B_{LISM} lies in the plane of the two flow vectors (the hydrogen deflection plane), which can push the TS closer to the Sun in the Southern Hemisphere, helping to explain why Voyager 2 (V2; -29° latitude) crossed the TS ~ 10 AU closer to the Sun than

¹Department of Astronomy, Boston University, Boston, MA 02215, USA. ²Space Research Centre of the Polish Academy of Sciences, 00-716 Warsaw, Poland. ³Kavli Institute, Massachusetts Institute of Technology, Cambridge, MA 02139, USA. ⁴Astronomical Engineering Division, University of Southern California, Los Angeles, CA 90089, USA. ⁵Institut für Astrophysik und Extraterrestrische Forschung, University of Bonn, 53115 Bonn, Germany. ⁶Institut für Theoretische Physik IV, Ruhr-Universität Bochum, 44780 Bochum, Germany. ⁷Department of Astronomy and Astrophysics, University of Chicago, Chicago, IL 60637, USA. ⁸Los Alamos National Laboratory, Los Alamos, NM 87545, USA. ⁹Lockheed Martin Advanced Technology Center, Palo Alto, CA 94304, USA. ¹⁰Department of Physics, University of Alabama, Huntsville, Alabama 35805, USA. ¹¹Department of Aeromechanics and Gas Dynamics, Moscow State University, and Space Research Institute (IKI) and Institute for Problems in Mechanics Russian Academy of Sciences, 117997 Moscow, Russia. ¹²Department of Physics, University of New Hampshire, Space Science Center, Durham, NH 03824, USA. ¹³Department of Space Science and Engineering, Southwest Research Institute, San Antonio, TX 78228, USA. ¹⁴Department of Physics, University of Texas at San Antonio, San Antonio, TX 78249, USA. ¹⁵NASA Goddard Space Flight Center, Greenbelt, MD 20771, USA. ¹⁶Department of Physics, University of Montana, Missoula, MT 59812, USA. ¹⁷Applied Physics Laboratory, Johns Hopkins University, Laurel, MD 20723, USA.

*To whom correspondence should be addressed. E-mail: nathanas@bu.edu